

# Novel percolation-based measure for fiber efficacy in fiber-reinforced concrete beams

Asghar Aryanfar<sup>1,2</sup>  | Irem Sanal<sup>2</sup>  | Jaime Marian<sup>3</sup>

<sup>1</sup>American University of Beirut, Riad El Solh, Beirut, Lebanon

<sup>2</sup>Bahçeşehir University, Istanbul, Turkey

<sup>3</sup>University of California, Los Angeles, California

## Correspondence

Asghar Aryanfar, American University of Beirut, Riad El Solh, Beirut 2020-1107, Lebanon.

Email: aryanfar@caltech.edu

## Abstract

Fiber-reinforced concrete exhibits a heterogeneous microstructure formed by aggregates, fibers and a matrix, where the stress from external forces can lead to cracking and fracture. This paper discusses the development of a computational measure for predicting the fiber's efficacy by means of the energy absorbed within the initiated area of the cracks. The analytical development was verified with experimental data from the literature and the results were justified with numerical simulations in the elastic regime. This development couples the localization of the stress in the crack tip with the random distribution of the cracks, which leads to the spatial strain field. Such percolation-based quantification of the cracks in the early-stage particularly is useful for effective utilization of fibers during the cracking progress.

## KEYWORDS

absorbed energy, fiber reinforcement, fracture, percolation

## 1 | INTRODUCTION

Fiber-reinforced concrete (FRC) is one of the most promising innovations of concrete technology. The addition of short, discrete fibers enhances the properties of this composite cement-based material.<sup>1,2</sup> The inclusion of steel fibers significantly improves the tensile behavior during microcracking by reducing their widths and spacing.<sup>3,4</sup> The bridging and stretched fibers increase the post-cracking residual strength of FRC and counter the crack propagation. Moreover, due to the de-bonding and pull-out mechanisms of the fibers, a greater amount of energy is dissipated, while improving the toughness significantly. This enhanced behavior is mainly influenced by the amount of bridging fibers and their mechanical properties, even at low dosages.<sup>5-8</sup>

In recent studies, the role of fiber orientation, distribution and pull-out/torsional behavior on the transferred stress for enhancing the postcracking flexural strength was determined<sup>9-11</sup> as well as a size effect.<sup>12</sup> Additionally, image processing and tomography techniques have been applied to monitor the role of fibers as a nondestructive method<sup>13-18</sup> and the crack patterns have been estimated from surfaces of the specimen.<sup>19</sup>

Fracture in FRC initially starts with the formation of microcracks, mainly due to inhomogeneity, anisotropy and stress localization of the composite. This process consumes a large amount of energy and slows down the propagation rate. The crack region can be divided into a frontal zone which is localized ahead of the main crack that forms the microcracks<sup>20</sup> and into a zone that includes the fracture surface. The load transfer is controlled either by bridging of fibers or their pull-out friction.<sup>21,22</sup> In the fiber-bridging zone, only the fibers carry postcracking loads taken by the composite.<sup>23,24</sup> Yet, more information from a versatile method on the quantitative load transferring capacity of fibers would highly benefit

Discussion on this paper must be submitted within two months of the print publication. The discussion will then be published in print, along with the authors' closure, if any, approximately nine months after the print publication.

Parameter	$L$	$W$	$H$	$a$	$\sigma_y$	$L_f$	$D_f$	$\Delta t$
Value	400	100	{26,39,65,100}	50	2000	{6,13}	0.16	15
Unit	mm	mm	mm	mm	MPa	mm	mm	s

**TABLE 1** Experimental parameters

the understanding of control of crack initiation and propagation.

In this paper, a new measure for the efficacy of the fibers in FRC is introduced using the initial area of the formed cracks. Such randomly fractured medium has been simulated using our percolation paradigm. The link between the geometry of the fracture zone and the mechanics (i.e., loading) is provided by distinguishing the original applied energy of loading to the specimen, which is stored as elastic energy, and the absorbed energies in the fibers during the inception of cracks. The method has been implemented to assess experimental data of four-point flexural loading. Tests have quantified the ability of the fibers to resist the cracks during any stage of the development and those results were verified with outcomes of recent studies in reported literature.

## 2 | METHODOLOGY

### 2.1 | Numerical computations

In order to validate the numerical computations developed in this study for determining the crack effectiveness of the fibers, the results of fiber-reinforced cementitious (FRCC) specimens of previous studies were adapted from literature.<sup>13,25</sup> The concrete mortar mixes were designed with a water-binder ratio of  $w/b = 0.42$  and 1.7% added dosage of superplasticizer with regard to cement weight. The cement-based mixture was a fabricated mortar mix with the following proportions by weight:

Cement : Sand : Slag : Water : Superplasticizer : Fibers  $\equiv$  98 : 1114 : 418 : 220 : 18 : 94.8.

where the cement type is CEM142.5R and the superplasticizer is polycarboxylate-based. The densities of these materials are 3.14, 2.65, 2.92, 1.0, and 7.85 g/cm<sup>3</sup>, respectively. The FRC mixes in this study were produced with a fiber volume fraction of 1.5% and cured for 28 days ( $RH > 90\%$ ,  $T = 20 \pm 2^\circ\text{C}$ ). Table 1 indicates the specimen length  $L$ , width  $W$ , height  $H$ , fibers length  $L_f$ , diameter  $D_f$  (aspect ratio  $\equiv$  {81.25, 37.5}), tensile stress  $\sigma_y$ , with the distance parameter  $a$  and the measurement time interval  $\Delta t$ .

The beam specimens were tested in four-point bending, according to Figure 1a, using a closed-loop

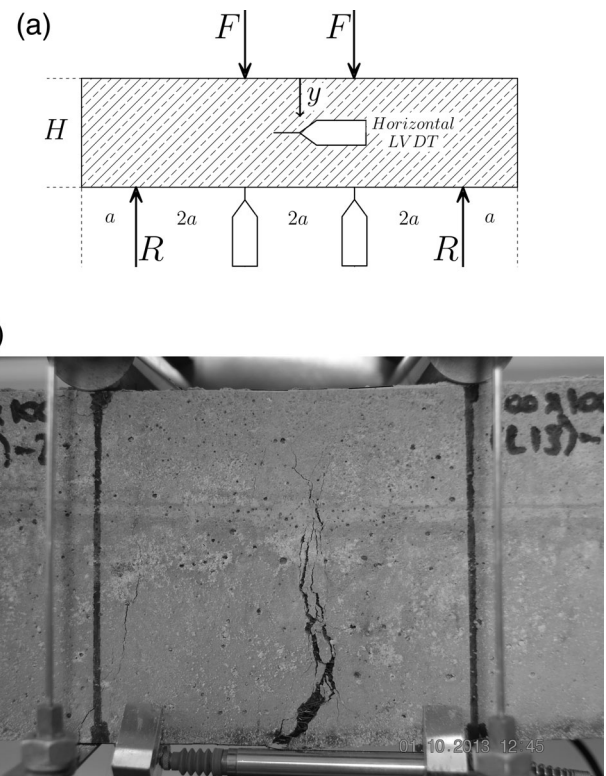


**FIGURE 1** Experimental procedure

displacement controlled servo hydraulic testing machine with a capacity of 100 kN.<sup>13,25</sup> Four linear variable displacement transducers (LVDTs) were mounted vertically under the specimen to measure the average deflection and two LVDTs were mounted horizontally on opposite sides of the loading region of the specimen to measure the average crack mouth opening displacement. These LVDTs also provided feedback to the servo-valve for closed-loop control of the test. For crack monitoring, a camera was placed perpendicular to the beam face at a distance of 38 cm from the specimen and the illumination was carried out using a white light projector. Successive digital images were taken from each beam specimen undergoing deformation using a high-resolution camera in successive intervals of  $\Delta t$ . The deformation and patterns obtained from images were compared with the original undeformed reference image to determine the change in the crack area and the local displacements according to the flowchart given in Figure 2. Loading was applied at a LVDT-controlled displacement rate of 0.01 mm/

**FIGURE 2** Flowchart for image processing method. The complete description of parameters is provided in Section 2.1 ( $\Delta A$ : incremental area;  $V$ : displacement vector;  $I$ : displacement value;  $Im^{k+1}$ : the image for the frame number  $k + 1$ )

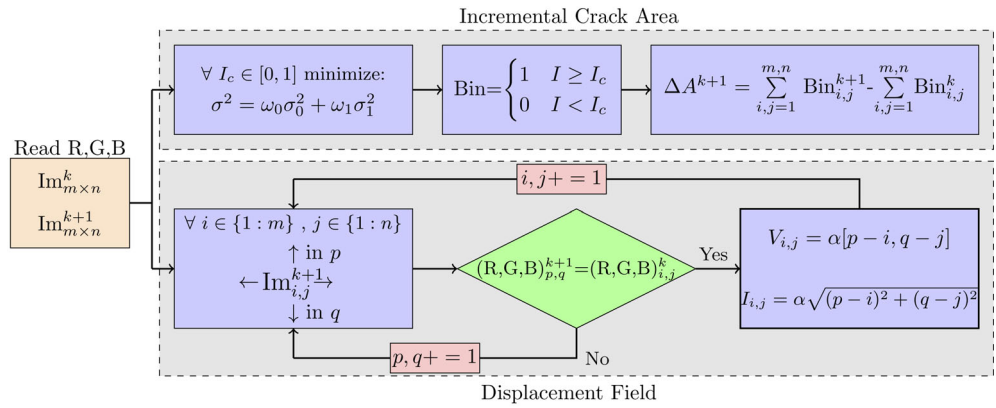
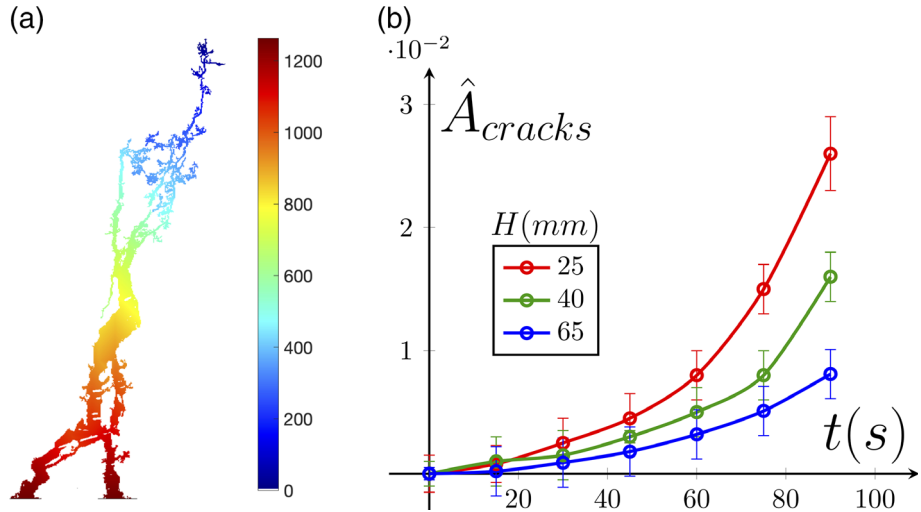


**FIGURE 3** Percolation-based computation and tracing of effective cracks



min, until the opening of the crack reached half the fiber length ( $w_{\max} \frac{L_f}{2}$ ). Such experimental data were used to identify the effective cracks as well as the displacement field within the sample in the period of time. The image processing steps, which are shown in the flowchart of Figure 2, are as follows:

(1) The bare image contains the information from the red, green, and blue values (i.e.,  $\{R, G, B\} \in [0, 255]$ ). This information can be transferred to a normalized gray-scale intensity image by averaging the values as:

$$I_{ij} = \frac{R_{ij} + G_{ij} + B_{ij}}{3 \times 255} \quad (1)$$

where the  $I_{i,j} \in [0, 1]$  is the intensity value of the obtained gray-scale image.

(2) The cracked regions (i.e., black) can be distinguished from solid mortar (i.e., white) by establishing a grayness threshold,  $I_c \in [0, 1]$ , which classifies matrix elements into black and white classes  $\{B, W\} \in (0, 1)$ . This

value is determined iteratively from Otsu's method by minimizing the intraclass variance  $\sigma^2$  as follows<sup>26,27</sup>:

minimize  $\sigma^2$  such that:

$$\begin{cases} \sigma^2 = \omega_1 \sigma_0^2 + \omega_2 \sigma_1^2 \\ \omega_1 + \omega_2 = 1 \end{cases} \quad (2)$$

where  $\omega_1$  and  $\omega_2$  are the fractions of black/white portions and  $\sigma_2^2$  are the corresponding variances for each classified zone. Minimization of intraclass variance  $\sigma^2$  ensures that the obtained binarized image provides the best approximation of the original gray-scale image as closest proximity for each chosen group is considered in the same class.

(3) The augmented area ( $\Delta A$ ) in each stage can be obtained by percolating (i.e., propagating) through the cracks from the bottom surface until no further progress is made.<sup>28</sup> The incremental area difference  $\Delta A^{k+1}$  can be obtained from the difference of two subsequent obtained

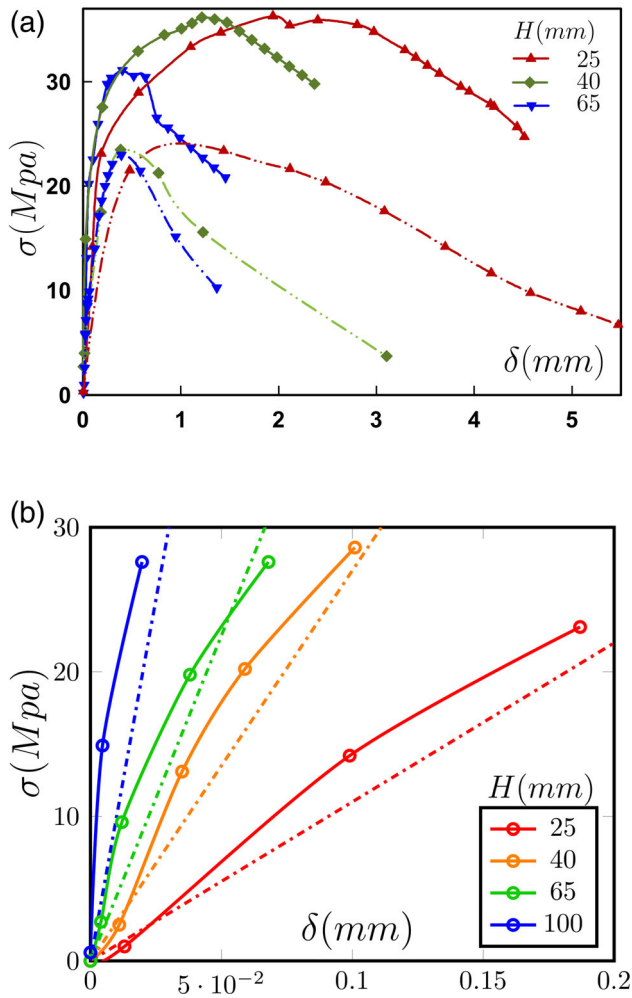


**FIGURE 4** Stress-displacement diagrams

images (i.e.,  $Im^k, Im^{k+1}$ ). Figure 3a represents the captured effective cracks computed by means of percolation method from the surface, in the horizontal and vertical directions (left, right, top, bottom). The values on the color-bar correlate with the distance from the instigation point of the cracks (i.e., surface).

Consequently, the normalized computed crack area is defined as a fraction of total surface area ( $\hat{A} := \frac{A_{cracks}}{A_{tot}}$ ) and is tracked versus time. Figure 3b represents such characterization, where the error-bars show the  $SD$  for three similar experimental setups for each point in the graph.

(4) The displacement field is obtained from tracking the  $\{R, G, B\}$  values of each element to its closest proximity and extracting the corresponding displacement vector  $V_{i,j}$  as well as displacement magnitude  $I_{i,j}$ .  $\alpha (\approx 2.5)$  is the scaling correction factor, relating the image value to the experimental magnitudes.

During these intervals the load  $F$  and the corresponding displacements  $\delta$  are recorded as well. Figure 4a represents the stress-displacement diagrams versus the height of the specimens and the fiber length, where the stress  $\sigma$  is simply

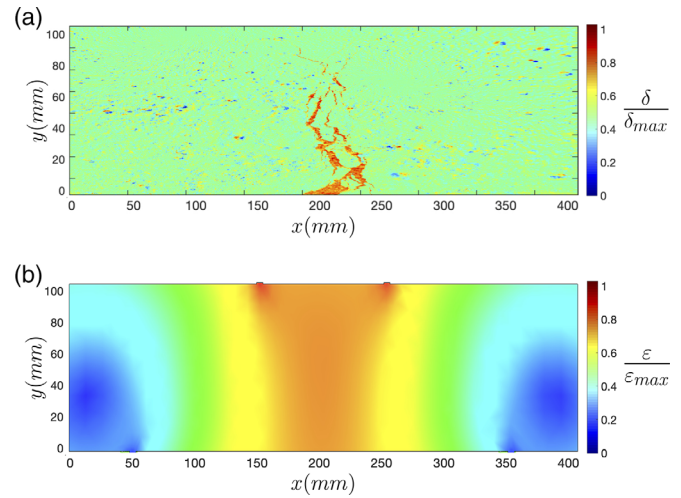


**FIGURE 5** Correlation between the experiments/simulations

computed with presumption of elastic behavior before the initiation of cracks ( $\sigma = \frac{Mc}{I}$ ). The curve for the height  $H = 100$  mm is omitted due to extreme slope to provide a clear appearance in this figure. Additionally, Figure 4b shows a comparison of the experimental curves in the linear regime. Each point represents the average of three experiments. The analytical relation between the stress  $\sigma$  and the deflections of the beam  $\delta_1$  and  $\delta_2$  in the measurement points are shown by Equation (3):

$$\delta_1 = \delta_2 = \frac{5a^2}{EH} \sigma \quad (3)$$

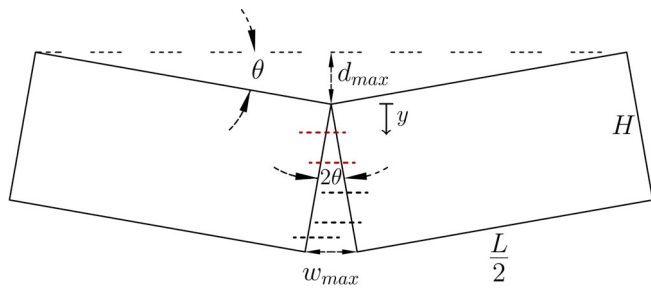
where the constants  $a$ ,  $E$ , and  $H$  are provided in Table 1 and the mathematical proof provided in the Supplemental Information. The resulting relation from this equation has also been added to Figure 4b.

Figure 5a represents the start-to-end displacement field representing the evolved cracks in the most distinguishable states (i.e., images). Each individual element in this figure is subtracted from the original bare image from the experiment and the color-bar distinguishes the cracks from the specimen medium.

Additionally, the numerical simulation on the identical condition of the experimental geometry, material and the loading system was performed with the SolidWorks simulation package and the obtained strain field in the linear regime was obtained for further analysis, which is shown in Figure 5b.

## 2.2 | Analytical modeling

Figure 6 shows the schematics of an ideal, symmetric, and full fracture for modeling and geometrical calculations. The acting fibers are shown in red while others became



**FIGURE 6** Geometric idealization of the beam specimen at complete fracture (for modeling)

inactive due to pull out. The fiber efficacy measure ( $\Lambda$ ) in fact takes into account the role of active fibers involved in effectively resisting the crack growth.<sup>29</sup> In the elastic stage, the average fiber stress correlates with the localized strain value before the formation of cracks. However, upon the fracture the strain field in the specimen is relaxed and the elongation of fibers is mostly consistent with the crack opening. Therefore, the efficacy measure  $\Lambda$  correlates with the local strain and consequently to the crack opening. Considering the geometry, during infinitesimal fracture, the opening of the crack  $w$  correlates with the vertical distance  $y$  from the crack tip as shown by Figure 6. For a typical crack instigated with a depth of  $y_0$ , due to geometry the crack area  $A_{cracks}$  is:

$$A_{cracks} = \int_{y_0}^H w(y) dy \quad (4)$$

Depending on if the fibers have reached yielding limit  $\sigma_y$ , they will either act elastic or plastic.

### 2.2.1 | Plastic zone

At a larger crack opening, the fibers are stretched up to the maximum (plastic) stress ( $\sigma[y] \approx \sigma_y$ ). For a crack ranging from the tip-to-toe in the span of  $y_0$  to  $H$ , the absorbed energy for the fiber  $\delta E_{fib, pl}$  would be:

$$\delta E_{fib, pl} = \sigma_y \delta A_{fib} w \quad (5)$$

where  $A_{fib}$  is the cross-sectional area of the fiber and can be expressed as  $A_{fib} = \frac{\pi}{4} d^2$  and  $w$  is the local crack opening. Therefore, the total absorbed energy of the fibers  $E_{fib}$  can be expressed as:

$$E_{fib, pl} = \frac{\pi d^2}{4} \sigma_y \sum_{i=1}^n w_i \quad (6)$$

where  $n$  is the total number of bridging fibers. As the fibers are highly packed, one can assume that they cover

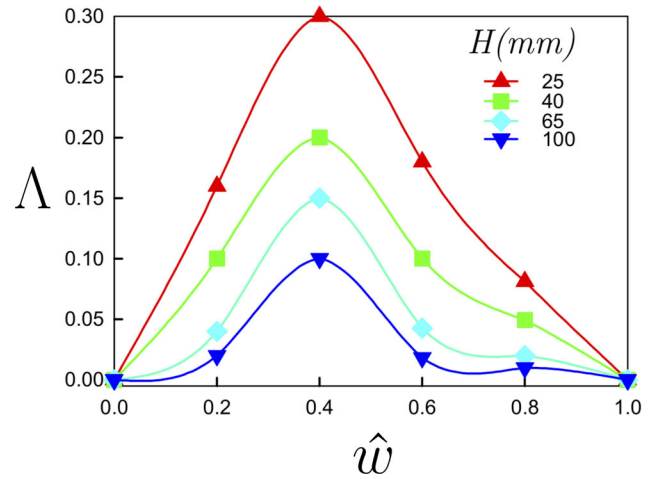


**FIGURE 7** Evolution of fiber efficacy  $\Lambda$  versus the normalized crack opening  $\hat{w}$

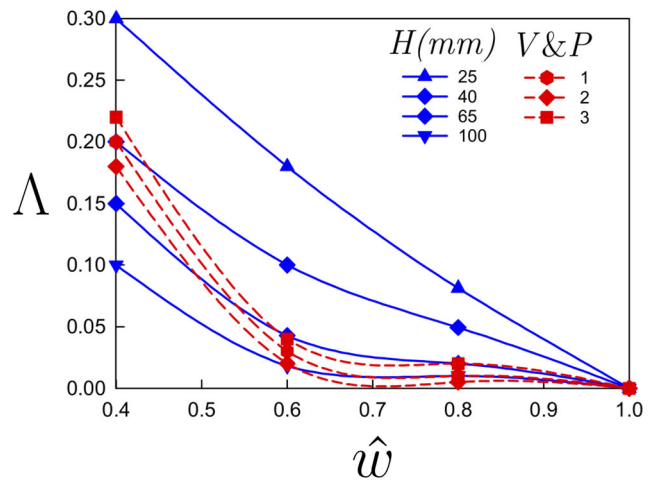


**FIGURE 8** Correlation of the fiber efficacy  $\Lambda$  with the literature

the entire surface area of the cracks. Therefore, since all the fibers have identical diameters and their large population covers the entire crack area, one can assume that  $d := dy$  and we arrive at the following for the energy absorbed in the fibers  $E_{fib}$ :

$$E_{fib, pl} = \frac{\pi d^2}{4} \sigma_y \int_{y_0}^H w(y) dy \quad (7)$$

Combining Equations (4) and (7) results in Equation (8)

$$E_{fib, pl} = \frac{\pi}{4} d^2 \sigma_y A_{cracks} \quad (8)$$

### 2.2.2 | Elastic zone

Below the yielding limit, for a crack opening with the tip at the depth of  $y_0$ , the following geometrical

relationship can be derived due to triangular inequality (Figure 6):

$$\frac{w(y)}{y-y_0} = \frac{w_{\max}}{H-y_0} \approx \frac{2d_{\max}}{L/2} \quad (9)$$

therefore, the individual strain of each fiber is expressed as:

$$\epsilon(y) = \frac{w(y)}{L_f} = \frac{4d_{\max}}{L_f L} (y-y_0) \quad (10)$$

and the energy absorbed by the individual fiber  $\delta E_{fib}$  becomes:

$$\delta E_{fib} = EA_{fib} \frac{16d_{\max}^2}{L_f L^2} (y-y_0)^2 \quad (11)$$

Thus, the total absorbed energy in fibers  $E_{fib, el}$  can be integrated as:

$$E_{fib,el} = \left( \frac{20EA_{fib}H^3}{3L_fL^2} \right) \delta^2 \quad (12)$$

The original energy  $E_{load}$  of the beam obtained by applying two external loads  $F$  during the experiment is:

$$E_{load} = 2F\delta \quad (13)$$

where  $\delta$  is the corresponding displacement measured from the gauges. Before the fracture, the entire work (i.e., energy) from the loads is stored elastically within the beam. However, after the fracture the rest of the beam is partially relaxed due to the opening of the cracks and the added energy is divided for the formation of the crack  $E_{crack}$  as well as the stretching of the fibers  $E_{fibers}$  as follows:

$$E_{load} = E_{crack} + E_{fibers} \quad (14)$$

which in fact proves that, the more the energy is transmitted by fibers the less crack surfaces form, which is also the case for hardening cementitious materials. Therefore, the fiber efficacy factor  $\Lambda$  should describe the fraction of the absorbed energy within the plastic deformation of the fibers:

$$\Lambda = \frac{E_{fib}}{E_{load}} \quad (15)$$

The typical yield strain of the fibers is very small and in the range of  $\epsilon_y \approx 0.001-0.002$ ,<sup>30</sup> therefore considering

the fiber strain range in the experiments, they mostly will be in the plastic deformation stage. Consequently, the evolution of fiber efficacy  $\Lambda$  versus the maximum crack development is calculated assuming the plastic behavior of all the fibers (Equation (8)) for the results shown by Figure 7, where the crack opening has been normalized to the fiber length as:  $\hat{w} = \frac{w}{L_f}$ . As well, the comparative study for the development of the cracks, after reaching the peak value, is shown in Figure 8. Nonetheless, the fibers in some cases contribute to an increasing crack surface (i.e., SHCC materials).<sup>31</sup>

### 3 | RESULTS AND DISCUSSIONS

While the heterogeneity of FRC allows for the initiation of cracks possibly in multiple locations, the cracks starting from the surface of the FRC specimen are the most prone for causing the failure with a large margin relative to other cracks. Such a crack can be captured in our computation via percolating from the bottom of the specimen until no further progress is made (Figure 3a). The dynamics of propagation of the effective cracks in Figure 3b represent quickening behavior. Few reasons cause such behavior including the augmentation of the flexural stress due to the reduction of cross section as the crack grows ( $\sigma = \frac{Mc}{I}$ ). During the crack growth the resisting cross-section decreases, which significantly reduces the second moment of area (i.e.,  $I \propto H^3$ ) and the flexural stress increases to a considerable extent. This causes rampant growth behavior in the cracks. For the same reason, the growth is the most sensitive to the specimens with the lower height. Nevertheless, if the FRC is in the plastic state in the zone with the highest flexural tensile stresses, the same quickening trend is expected due to inverse correlation with the effective area  $A$  which continuously decreases, where for the completely plastic state:  $M = F \frac{d}{2} = \sigma_y \frac{AH}{2}$  and therefore:

$$\sigma_y = \frac{4M}{AH} \quad (16)$$

The stress-displacement relations shown in Figure 4a reveal new information on the role of the fiber length and geometry on the mechanical behavior. The reduction of the ultimate flexural strength versus the height of the beams reveals the deflection-softening behavior, whereas the initiation point of first cracking remains the same as it represents the matrix performance. On the contrary, indicating the deflection-hardening behavior has been observed in the beams with less height, representing the role of size effect.<sup>32</sup> The energy absorption (i.e., toughness) and deflection-hardening capacities both

decreased at increasing beam height. The peaking of the load during the experiment shows the toughening mechanism at the crack tip zone. The fibers become less effective at a larger beam height, especially this is pronounced at the peak of the load, where cracks become localized.

The comparison of the analytical and experimental trends shown in Figure 4b reveals that in the experiments a slightly higher strength is obtained (i.e., elastic modulus) compared to the analytical prediction for pure mortar. This is simply due to the existence of the fibers embodied within the mortar, which in fact acts as a composite materials as a whole. In fact, the observed differences indicate that the fibers are already active even before the initiation of the cracks.

Analysis of the displacement diagram for the experimental cracked specimen in Figure 5a versus the computation of the strain map in the elastic regime in Figure 5b reveals the consistency of the critical state in the middle bottom of the specimen, which is under tension. We note the highest localized strain values precisely under the loading points in Figure 5b, which are not critical since those locations are under compressive stress.


Before crack initiation, the role of the fibers is in terms of the elastic shear transfer with the matrix. However, upon the initiation of the cracks, the tensile behavior is activated and add up to the flexural resistance, leading to a ductile behavior.<sup>33</sup> Their effectiveness relies on the bridging within the formed crack. The number of activated fibers increases with further crack propagation and the fiber efficacy factor increases as shown in Figure 7. However, upon extended crack opening, the fibers with shorter embedment lengths from one of the ends (at least) are successively pulled out and do not contribute any longer to the propagation resistance. Due to crack geometry, the frequency of such fibers decreases from the crack tip until the limit where the longest embedded fiber is pulled out (Figure 6). The inception of the pull-out process can be distinguished by locating the peaks of fiber efficacy  $\Lambda$  in the Figure 7, which occurs at  $w \sim 0.4L_f$ . This correlates highly with the reported value of embedment length for effective bridging of  $w_{\max} < 0.5L_f$ ,<sup>34–36</sup> where the maximum number of the fibers is effectively bridging the crack. Nonetheless, the slightly lower value compared to the value obtained in this development shows that a small fraction of the fibers could in fact be pulled out before reaching this typical value. Additionally, the lower values of the experimental measurements relative to the model could be explained with the role of fiber orientation since the modeling assumption is horizontal fibers whereas in the experiments a projection of the force of the fibers will in fact hold the crack opening and the reported fiber orientation coefficient has been indicated as  $\approx 0.65–0.7$ .<sup>37–39</sup>

After reaching the maximum value, the fiber efficacy measure  $\Lambda$  decreases with progressing crack opening, as shown in the right half of Figure 7 and reaches zero in the limit where the crack width approaches the fiber length ( $w \approx L_f$ ). This can explain the pull-out process and correlates highly with the reported values<sup>40</sup> as shown in Figure 8. Nevertheless, the slightly higher values in Figure 8 can be due to the assumption of complete yielding and bridging in the fibers, which is more effective than frictional and pull-out contributions. Such decreasing trend for the fibers' effectiveness versus crack progress has been previously reported as well.<sup>41–43</sup> Additionally, it is observed that the thinner beams show better fiber-performance in Figure 7. The underlying reason can be related to the formation of less cracked regions in the thinner beams and therefore less fracture energy is needed. Thus, from Equation (14) the rest of the energy gets absorbed by the fibers, which is higher in the thinner beams. Needless to mention that the curvature trend in Figure 8 interestingly correlates with the literature as well, which is more pronounced in the right half (i.e., postcrack behavior) of Figure 7.

## 4 | CONCLUSIONS

In this paper, a new measure  $\Lambda$  was introduced for the quantification of the effectiveness of fibers in FRC during the full course of crack instigation and propagation. Percolation-based modeling was performed for computing the effective area of the cracks and a model was established based on the absorbed energy of the fibers. Upon the instigation of the infinitesimal cracks and activation of the fibers, the fiber efficacy has increased and reached a maximum value. After the pull-out process, the efficacy value decreased, concurrent in the literature. The better performance of the beams with a smaller heights represents more proper spatial orientation of fibers, leading to effective bridging. The developed measure can be used to quantify fibers' performance in FRC beams versus cracks area for any propagation patterns.

### ORCID

Asghar Aryanfar  <https://orcid.org/0000-0002-8890-077X>

Irem Sanal  <https://orcid.org/0000-0003-1682-1789>

### REFERENCES

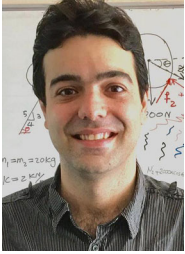
1. Di Prisco M, Plizzari G, Vandewalle L. Fibre reinforced concrete: New design perspectives. *Mater Struct.* 2009;42(9): 1261–1281.

2. Walraven JC. High performance fiber reinforced concrete: Progress in knowledge and design codes. *Mater Struct.* 2009;42(9):1247.
3. Grzybowski M, Shah SP. Shrinkage cracking of fiber reinforced concrete. *Mater J.* 1990;87(2):138–148.
4. Banthia N, Azzabi M, Pigeon M. Restrained shrinkage cracking in fibre-reinforced cementitious composites. *Mater Struct.* 1993;26(7):405–413.
5. Bentur A, Mindess S. *Fibre reinforced cementitious composites.* Florida, FL: CRC Press, 2014.
6. Löfgren I. *Fibre-reinforced concrete for industrial construction—A fracture mechanics approach to material testing and structural analysis.* Göteborg, Sweden: Chalmers University of Technology, 2005.
7. Romualdi JP, Mandel JA. Tensile strength of concrete affected by uniformly distributed and closely spaced short lengths of wire reinforcement. *J Proc.* 1964;61:657–672.
8. Ong KCG, Paramasivam P. Cracking of steel fibre reinforced mortar due to restrained shrinkage. *Fibre reinforced cements and concretes: Recent developments, 1989;* p. 179–187.
9. Alam SY, Saliba J, Loukili A. Fracture examination in concrete through combined digital image correlation and acoustic emission techniques. *Constr Build Mater.* 2014;69:232–242.
10. Shah SG, Kishen JMC. Fracture properties of concrete–concrete interfaces using digital image correlation. *Exp Mech.* 2011;51(3):303–313.
11. Okay F, Engin S. Torsional behavior of steel fiber reinforced concrete beams. *Construct Build Mater.* 2012;28(1):269–275.
12. Ghasemi M, Ghasemi MR, Mousavi SR. Studying the fracture parameters and size effect of steel fiber-reinforced self-compacting concrete. *Construct Build Mater.* 2019;201:447–460.
13. Şanal İ, Zihnioğlu NÖ, Hosseini A. Particle image velocimetry (PIV) to evaluate fresh and hardened state properties of self compacting fiber-reinforced cementitious composites (SC-FRCCS). *Construct Build Mater.* 2015;78:450–463.
14. Hosseini A, Mostofinejad D, Hajialilue-Bonab M. Displacement and strain field measurement in steel and rc beams using particle image velocimetry. *J Eng Mech.* 2014;140(11):04014086.
15. Sanal I. Understanding global mechanical response of fiber reinforced cementitious composite beams from local fracture process. *Struct Control Health Monit.* 2018;25(8):e2202.
16. Ponikiewski T, Gołaszewski J, Rudzki M, Bugdol M. Determination of steel fibres distribution in self-compacting concrete beams using X-ray computed tomography. *Arch Civil Mech Eng.* 2015;15(2):558–568.
17. Balázs GL, Czoboly O, Lublós É, Kapitány K, Barsi Á. Observation of steel fibres in concrete with computed tomography. *Construct Build Mater.* 2017;140:534–541.
18. Şanal İ. Evaluating the effects of various factors on mechanical performance of SC-FRCCS [PhD thesis]; 2015.
19. Jansson A, Flansbjerg M, Löfgren I, Lundgren K, Gylltoft K. Experimental investigation of surface crack initiation, propagation and tension stiffening in self-compacting steel–fibre-reinforced concrete. *Mater Struct.* 2012;45(8):1127–1143.
20. Bradt RC. Problems and possibilities with cracks in ceramics. In: Carlsson R, Karlsson S, editors. *Proc. 11th International Conf. on Science of Ceramics held at Stenungsund, Sweden, June 14–17, 1981.* Gothenburg, Sweden: Swedish Ceram. Soc., 1981; p. 349.
21. Zhan-Qiao W. Testing research on the fracture properties of fiber reinforced high-strength concrete [PhD thesis]. Zhengzhou University; 2004.
22. Pimentel M, Abrishambaf A, Nunes S. Anisotropic tensile behaviour of UHPFRC: Meso-scale model and experimental validation; 2019.
23. Lu T-q, Long J-j. The application of synthetic fibers in concrete. *J Suzhou Inst Silk Text Technol.* 2005;2:010.
24. Guo Y-c, Hong-Zhou Z. Research and engineering applications of fiber-reinforced concrete. *Guangdong Build Mater.* 2004;7:8–9.
25. Şanal İ, Özyurt N, Hosseini A. Characterization of hardened state behavior of self compacting fiber-reinforced cementitious composites (SC-FRCC's) with different beam sizes and fiber types. *Compos Part B Eng.* 2016;105:30–45.
26. Otsu N. A threshold selection method from gray-level histograms. *Automatica.* 1975;11(285–296):23–27.
27. Aryanfar A, Hoffmann MR, Goddard WA III. Finite-pulse waves for efficient suppression of evolving mesoscale dendrites in rechargeable batteries. *Phys Rev E.* 2019;100(4):042801.
28. Aryanfar A, Goddard W III, Marian J. Constriction percolation model for coupled diffusion-reaction corrosion of zirconium in PWR. *Corros Sci.* 2019;158:108058.
29. Krenchel H. Fibre spacing and specific fibre surface; 1975.
30. Behera BK, Hari PK. 7-Tensile behavior of woven fabrics. *Woven Text Struct.* 2010;137–163.
31. Gideon PAG, Zijl V, Wittmann FH. *Durability of strain-hardening fibre-reinforced cement-based composites (SHCC).* Vol 4. Springer Science & Business Media, 2010.
32. Nguyen DL, Kim DJ, Ryu GS, Koh KT. Size effect on flexural behavior of ultra-high-performance hybrid fiber-reinforced concrete. *Compos Part B Eng.* 2013;45(1):1104–1116.
33. Pfyl T. *Tragverhalten von Stahlfaserbeton.* Vol 279. vdf Hochschulverlag AG, 2003.
34. Fehling E, Schmidt M, Walraven J, Leutbecher T, Fröhlich S. *Ultra-high performance concrete UHPC: Fundamentals, design, examples.* John Wiley & Sons, 2014.
35. Rossi P, Chanvillard G. *5th rilem symposium on fibre reinforced concretes (BEFIB 2000).* Cachan, France: RILEM Publications, 2000.
36. de Oliveira FL. *Design-oriented constitutive model for steel fiber reinforced concrete.* Barcelona, Spain: Universitat Politècnica de Catalunya, 2010.
37. Kang S-T, Kim J-K. The relation between fiber orientation and tensile behavior in an ultra high performance fiber reinforced cementitious composites (UHPFRC). *Cem Concr Res.* 2011;41(10):1001–1014.
38. Kang ST, Lee BY, Kim J-K, Kim YY. The effect of fibre distribution characteristics on the flexural strength of steel fibre-reinforced ultra high strength concrete. *Construct Build Mater.* 2011;25(5):2450–2457.
39. Martinie L, Roussel N. Simple tools for fiber orientation prediction in industrial practice. *Cem Concr Res.* 2011;41(10):993–1000.
40. Vougioukas E, Papadatou M. A model for the prediction of the tensile strength of fiber-reinforced concrete members, before and after cracking. *Fibers.* 2017;5(3):27.
41. Sorensen CO, Berge EA, Saga PE, Østvold A. Factors affecting the efficiency of fibers in concrete on crack reduction. *Open J Civil Eng.* 2013;3(02):80.
42. Buratti N, Mazzotti C, Savoia M. Post-cracking behaviour of steel and macro-synthetic fibre-reinforced concretes. *Construct Build Mater.* 2011;25(5):2713–2722.



43. Baltay P, Gjelsvik A. Coefficient of friction for steel on concrete at high normal stress. *J Mater Civ Eng*. 1990;2(1):46–49.

## AUTHOR BIOGRAPHIES



**Asghar Aryanfar**, is Assistant Professor of Mechanical Engineering at American University of Beirut. He received PhD from California Institute of Technology, Pasadena, CA in 2015 and his research is on the multiphysical modeling of nonlinear events in heterogenous media.



**Irem Sanal**, is Assistant Professor of Civil Engineering at Bahcesehir University, Istanbul, Turkey. She received her PhD from Bogazici University and her research is on fibre reinforced and sustainable concrete, crack monitoring, and environmental impacts.



**Jaime Marian**, is Associate Professor of Material Science and Mechanical Engineering at University of California, Los Angeles (UCLA). His research interest is Computational Material Science and Solid Mechanics.

## SUPPORTING INFORMATION

Additional supporting information may be found online in the Supporting Information section at the end of this article.

**How to cite this article:** Aryanfar A, Sanal I, Marian J. Novel percolation-based measure for fiber efficacy in fiber-reinforced concrete beams. *Structural Concrete*. 2020;1–9. <https://doi.org/10.1002/suco.201900362>